Shang, Z.; Hashemi, A.; Berencen, Y.; Komsa, H-P; Erhart, P.; Zhou, S.; Helm, M.; Krasheninnikov, A.; Astakhov, G.

Local vibrational modes of Si vacancy spin qubits in SiC

Published in:
Physical Review B

DOI:
10.1103/PhysRevB.101.144109

Published: 30/04/2020

Document Version
Publisher's PDF, also known as Version of record

Please cite the original version:
Shang, Z., Hashemi, A., Berencen, Y., Komsa, H.-P., Erhart, P., Zhou, S., Helm, M., Krasheninnikov, A., & Astakhov, G. (2020). Local vibrational modes of Si vacancy spin qubits in SiC. *Physical Review B*, *101*(14), Article 144109. https://doi.org/10.1103/PhysRevB.101.144109

Local vibrational modes of Si vacancy spin qubits in SiC

Z. Shang,[1,5] A. Hashemi,[2] Y. Berencén,[1] H.-P. Komsa,[2,3] P. Erhart,[4] S. Zhou,[1] M. Helm,[1,5] A. V. Krasheninnikov,[1,2] and G. V. Astakhov[1,*]

[1]*Institute of Ion Beam Physics and Materials Research, Helmholtz-Zentrum Dresden-Rossendorf, 01328 Dresden, Germany*
[2]*Department of Applied Physics, Aalto University, 00076 Espoo, Finland*
[3]*Microelectronics Research Unit, University of Oulu, 90014 Oulu, Finland*
[4]*Department of Physics, Chalmers University of Technology, 41296 Gothenburg, Sweden*
[5]*Technische Universität Dresden, 01062 Dresden, Germany*

(Received 5 February 2020; revised manuscript received 28 March 2020; accepted 31 March 2020; published 30 April 2020)

Silicon carbide is a very promising platform for quantum applications because of the extraordinary spin and optical properties of point defects in this technologically friendly material. These properties are strongly influenced by crystal vibrations, but the exact relationship between them and the behavior of spin qubits is not fully investigated. We uncover the local vibrational modes of the Si vacancy spin qubits in as-grown 4H-SiC. We apply microwave-assisted spectroscopy to isolate the contribution from one particular type of defects, the so-called V2 center, and observe the zero-phonon line together with seven equally separated phonon replicas. Furthermore, we present first-principles calculations of the photoluminescence line shape, which are in excellent agreement with our experimental data. To boost up the calculation accuracy and decrease the computation time, we extract the force constants using machine-learning algorithms. This allows us to identify the dominant modes in the lattice vibrations coupled to an excited electron during optical emission in the Si vacancy. A resonance phonon energy of 36 meV and a Debye-Waller factor of about 6% are obtained. We establish experimentally that the activation energy of the optically induced spin polarization is given by the local vibrational energy. Our findings give insight into the coupling of electronic states to vibrational modes in SiC spin qubits, which is essential to predict their spin, optical, mechanical, and thermal properties. The approach described can be applied to a large variety of spin defects with spectrally overlapped contributions in SiC as well as in other three- and two-dimensional materials.

DOI: 10.1103/PhysRevB.101.144109

I. INTRODUCTION

Since the demonstration of promising quantum properties of intrinsic point defects in silicon carbide (SiC) [1–4], they have been used to implement room-temperature quantum emitters [5–9] as well as to realize quantum sensing of magnetic fields [10–16], electric fields [17], and temperature [10,18,19]. Particularly, silicon vacancies (V_{Si}) and silicon-carbon divacancies (VV) in SiC reveal extremely long spin coherence time [7,8,16,20–25] and hold promise to implement quantum repeaters due to inherent spin-photon interface and high spectral stability [26–30]. Existing device fabrication protocols on the wafer scale in combination with three-dimensional (3D) defect engineering [31–33] allow manufacturing integrated quantum devices [34–37] with electrical [38–40] and mechanical [39,41,42] control of defect spin qubits. SiC nanocrystals with color centers are also suggested as fluorescence biomarkers in biomedical applications [43,44].

Vacancies can be imagined as artificial atoms incorporated into the SiC lattice. The communication with them is usually realized through optical excitation and photoluminescence (PL) detection. A fingerprint of each defect at cryogenic temperatures is the spectrally narrow emission at a certain wavelength, the so-called zero-phonon line (ZPL) [1,9,45,46]. Unlike atoms, radiative recombination in point defects is accompanied by phonon emission due to the interaction with lattice vibrations. This process results in the phonon side band (PSB), which is spectrally shifted towards longer wavelength relative to the ZPL [47,48]. A high ratio of the emitted light from the ZPL to the all emitted light, the Debye-Waller (DW) factor, is necessary for the implementation of quantum repeaters. The local vibrational energy also contributes to the spin-lattice relaxation time T_1 [24].

Although the understanding of the PSB is important for quantum applications, it has not been investigated systematically in SiC. The previous works [49,50] are limited to the report of the upper limit for the DW factor in a single V_{Si} defect, which is below 30%–40% depending on the crystallographic site and polytype. Most of the theoretical works are concentrated on the spin-optical properties [51–53].

In this work, we present the measurement of the V_{Si} PL spectrum in polytype 4H-SiC, consisting of the ZPL and seven increasingly broadened phonon replicas. There are two V_{Si} defects in 4H-SiC associated with different crystallographic environments, V1 and V2 [45,54]. Here, we concentrate on the V2 V_{Si} defect. We use microwave (MW)-assisted

*g.astakhov@hzdr.de

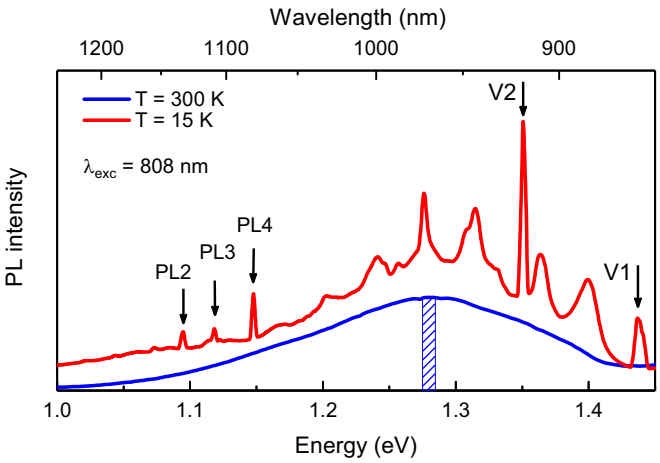

FIG. 1. Room-temperature and low-temperature PL from V_{Si} in pristine 4H-SiC. At $T = 300$ K, the shadow area around 970 nm indicates the spectral resolution $\Delta\lambda = 5.5$ nm. At $T = 15$ K, the zero-phonon lines of two distinct V_{Si} centers, V1 (ZPL at 863 nm) and V2 (ZPL at 918 nm), are clearly observed. The spectral resolution is $\Delta\lambda = 1.2$ nm ($\approx$ 2meV).

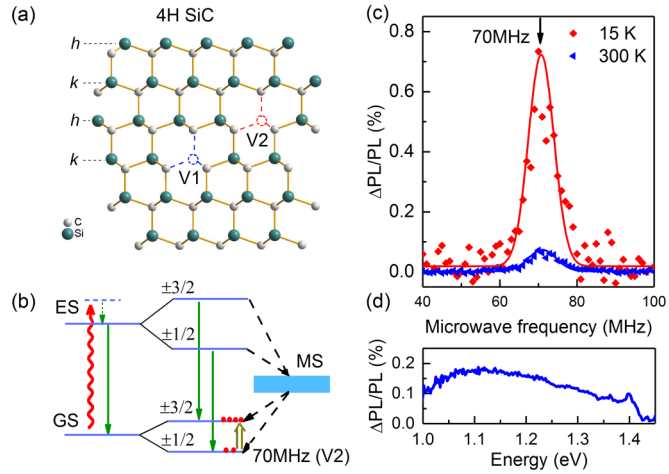

FIG. 2. (a) Schematic representation of the V1 and V2 V_{Si} defects associated with different crystallographic sites in 4H-SiC, according to [45]. (b) A scheme of the V2 spin pumping process. The red line presents the V2 spin center excited by an 808-nm laser. It relaxes to the ground state by two processes: radiative recombination (solid lines) and spin-dependent relaxation through the metastable states (MS) (dashed lines). The double arrow shows spin manipulation by the MW field at 70 MHz. (c) The V2 ODMR spectrum at room temperature and low temperature. The arrow indicates the resonance frequency of 70 MHz at zero magnetic field. (d) The V2 ODMR contrast at 70 MHz as a function of detection energy over the PL spectrum at room temperature.

spectroscopy and optically detected magnetic resonance (ODMR) to clearly separate spectrally overlapped contributions from other V_{Si} and VV defects. This approach allows us to unambiguously determine the V2 local vibrational energy. To shed more light on the microscopic nature of the PSB, we calculate the line shape using density functional theory (DFT). The experimental line shape is very well reproduced and concurrently also leads to close values for the DW factor and the local vibrational energy.

II. EXPERIMENT

The samples are excited with an 808-nm laser, which is modulated by a chopper at 20 Hz. An InGaAs detector converts the PL intensity into a photovoltage, which is amplified and read out by a lock-in amplifier. For the ODMR measurements, the chopper is removed and a commercial signal generator provides MW modulated at 20 Hz. The MW field guided into a coplanar waveguide induces spin transitions in the sample placed on the top of the waveguide. The modulated ΔPL signal is read out by a lock-in amplifier and hence presented in meV.

The sample under study is a piece diced from a pristine high-purity semi-insulating (HPSI) 4H-SiC wafer purchased from Cree. It is not irradiated and contains native V_{Si} and VV defects. The sample is mounted on the cold finger of a closed-cycle cryostat and the experiments are performed in the temperature range from $T = 300$ K down to $T = 15$ K. To increase the PL intensity at $T = 300$ K, we use a relatively wide monochromator entrance slit of 2 mm with a corresponding spectral resolution of 5.5 nm. At $T = 15$ K, the entrance slit size is reduced to 0.5 mm to improve the spectral resolution to 1.2 nm.

Typical PL spectra of the sample under study are presented in Fig. 1. A wide emission band with the maximum at around 1.28 eV (970 nm), associated with the V_{Si} defects [45], is clearly observed at $T = 300$ K. The emission band transfers to a series of ZPLs when the sample is cooled down to $T = 15$ K. Two ZPLs at 1.44 eV (863 nm) and 1.35 eV (918 nm) correspond to the V1 and V2 V_{Si} defects, respectively [9,45]. Several other ZPLs (labeled as PL2–PL4) are observed in the spectral range 1.1–1.2 eV and related to the silicon-carbon VV defects [46].

We concentrate on the V2 V_{Si} defect, associated with one of the two possible crystallographic sites in 4H-SiC [Fig. 2(a)]. The mechanism of the zero-field ODMR associated with the V_{Si} defects is qualitatively explained in Fig. 2(b). The V_{Si} has spin $S = 3/2$ in the ground state (GS) and the excited state (ES) [5]. Optical excitation of the V2 V_{Si} defect into the ES is followed by two processes, radiative recombination to the ground state GS (solid lines) and nonradiative spin-dependent relaxation (dashed lines) through the metastable state (MS). Application of the resonant MW field at 70 MHz, which is equal to the zero-field splitting between the $m_S = \pm 1/2$ and $m_S = \pm 3/2$ states, changes the population of these spin sublevels. It breaks the equilibrium between the relaxation processes resulting in nonzero ΔPL [10].

Figure 2(c) presents the ODMR contrast (ΔPL/PL) as a function of MW frequency. The PL is detected at 970 nm at $T = 300$ K (shaded area in Fig. 1) and at the V2 ZPL at $T = 15$ K. To ensure that ODMR experiments are performed under optimum conditions, we investigate the laser power and MW power dependencies at different temperatures. The ODMR contrast saturates in both cases [25] and we obtain $C_{max} = 0.80 \pm 0.02\%$ and $C_{max} = 0.21 \pm 0.05\%$ for $T = 15$ K and $T = 300$ K, respectively [Fig. 2(c)]. Remarkably, the ODMR

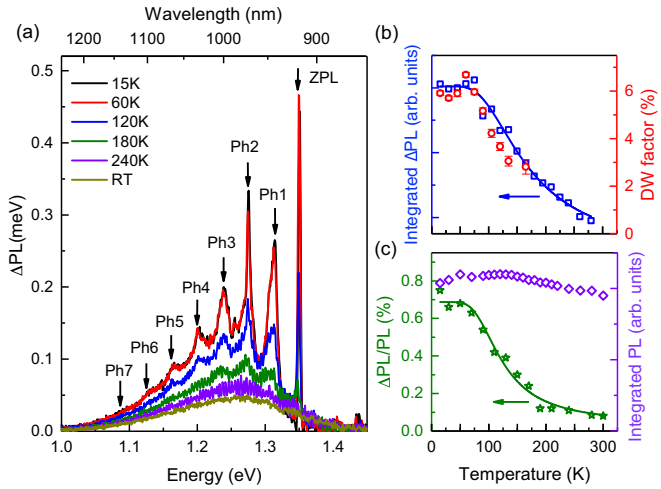

FIG. 3. (a) Evolution of the ΔPL spectrum with temperature under applied MW field at 70 MHz. (b) Temperature dependence of the spectrally integrated V2 ΔPL and the DW factor. The solid line is a fit to Eq. (1) with the activation energy $E_A = 39 \pm 4$ meV. (c) Temperature dependence of the ODMR contrast ΔPL/PL detected at the V2 ZPL and the integrated PL. The solid line is a fit to Eq. (1) with the activation energy $E_A = 39 \pm 3$ meV and ΔPL(0) replaced with ΔPL/PL(0).

contrast only marginally depends on the detection energy over the PL band (1.1–1.35 eV) at room temperature [Fig. 2(d)]. This is an indication that both spin states couple to phonons in the same way. A possible explanation is weak spin-orbit coupling [55], but a theoretical consideration of the spin polarization through intersystem crossing [56] involving local vibronic states is necessary to confirm this.

Next, we analyze how the change in the V2 ΔPL emission induced by the MW depends on the detection wavelength. We set the MW frequency to 70 MHz [Fig. 2(c)], and the ΔPL spectrum at $T = 300$ K is presented in Fig. 3(a). With decreasing temperature, the ΔPL spectrum transfers to the ZPL and the PSB consisting of seven equally separated phonon replicas (Ph1 – Ph7). These spectra differ from the PL spectrum presented in Fig. 1, which is composed of overlapping contributions from different defects. Especially, the V1 and V2 PSBs are merged together, making their separation difficult. In the ΔPL measurements, the MW frequency of 70 MHz is in the V2 spin resonance and, therefore, only the V2 PSB appears.

The spectrally integrated V2 ΔPL as a function of temperature is presented in Fig. 3(b). The experimental data can be well reproduced using a single activation energy [57]:

$$\Delta\mathrm{PL}(T) = \frac{\Delta\mathrm{PL}(0)}{1 + C\exp(-E_A/k_B T)}. \quad (1)$$

We obtain from the best fit [solid line in Fig. 3(b)] the activation energy $E_A = 39 \pm 4$ meV, which is equal within the experimental uncertainty to the local vibrational energy $\Delta E_{\mathrm{exp}} = 37 \pm 4$ meV, as discussed hereafter. The unitless coefficient $C = 9 \pm 2$ is determined by the ratio of different relaxation rates [57]. The ΔPL is contributed by the spin polarization and the PL intensity. In order to separate these contributions, we plot in Fig. 3(c) ΔPL/PL detected at the ZPL and the spectrally integrated PL. The experimental data for ΔPL/PL can be also well fitted to Eq. (1) with the activation energy $E_A = 39 \pm 3$ meV and ΔPL(0) replaced with $\Delta\mathrm{PL}/\mathrm{PL}(0) = 0.7\%$. This indicates that the integrated PL intensity of the V2 V_{Si} is nearly temperature independent up to 300 K. Indeed, this is in agreement with the integrated PL of Fig. 3(c), where a small decrease with rising temperature can be attributed to the contribution of other defects with stronger temperature dependence.

Figure 3(a) clearly shows the PSB extends below 1.1 eV (above 1150 nm). Thus, the DW above 30% found in earlier experiments [50] is definitely overestimated. Spectral integration of the experimental data in Fig. 3(a) [Fig. 4(b) shows a zoom-in of the V2 ZPL] results in the DW factor of about 6% for $T < 60$ K. This value should be corrected by the spectrally dependent readout contrast. Given the ΔPL/PL spectral dependence of Fig. 2(d), the expected value for the DW factor falls between 6% and 9%. The DW decreases with temperature as shown in Fig. 3(b). As the DW factor gives the fraction of elastic scattering, the temperature reduction can be attributed to the thermal motion effect [58] and multiphonon contributions.

We determine the local vibrational energy as the separation between two adjacent phonon peaks in $\Delta E_{\mathrm{exp}} = 37$ meV as presented in Fig. 4(a). The PSB formation is schematically presented in Fig. 4(c). The radiative recombination between the ES and the GS is accompanied by phonon emission. The energy dispersion of these phonons differs from the bulk phonon dispersion because of the broken translation symmetry in the vicinity of the V_{Si} defect. In the next section, we present detailed theoretical analysis of the local vibrational modes.

III. THEORY

We carried out DFT calculations as implemented in VASP [59] code to determine defect properties, configurational coordinate diagrams, and vibrational modes which finally allowed us to evaluate the PL line shape. A plane wave basis with a cutoff energy of 450 eV was employed to represent the electronic wave functions. All structural relaxations and the vibrational properties were calculated using the PBEsol [60] exchange-correlation functional. The geometry optimization continues until the energy differences and ionic forces are converged to less than 10^{-6} eV and 0.01 eV/Å, respectively. The PL line shape is calculated using the approach described in Ref. [48] and described in more detail below, which requires evaluation of the phonon spectra of the defective systems, but obtaining converged spectra requires large supercells that are computationally very demanding. Here, to speed up phonon calculations, the HIPHIVE [61] package was used to extract interatomic force constants (IFCs). Second-order IFCs were constructed using the recursive feature elimination optimizer by including pairs and triplets up to 4.2 and 3.6 Å, respectively. The modeled IFCs result in the validation root-mean-squared error of 13 meV/Å. The phonon frequencies and eigenvectors were finally assessed using PHONOPY software [62]. To adjust the energy scales, i.e., the band gap and the position of the defect levels within, we additionally used HSE06 [63] to calculate total energies and Kohn-Sham levels.

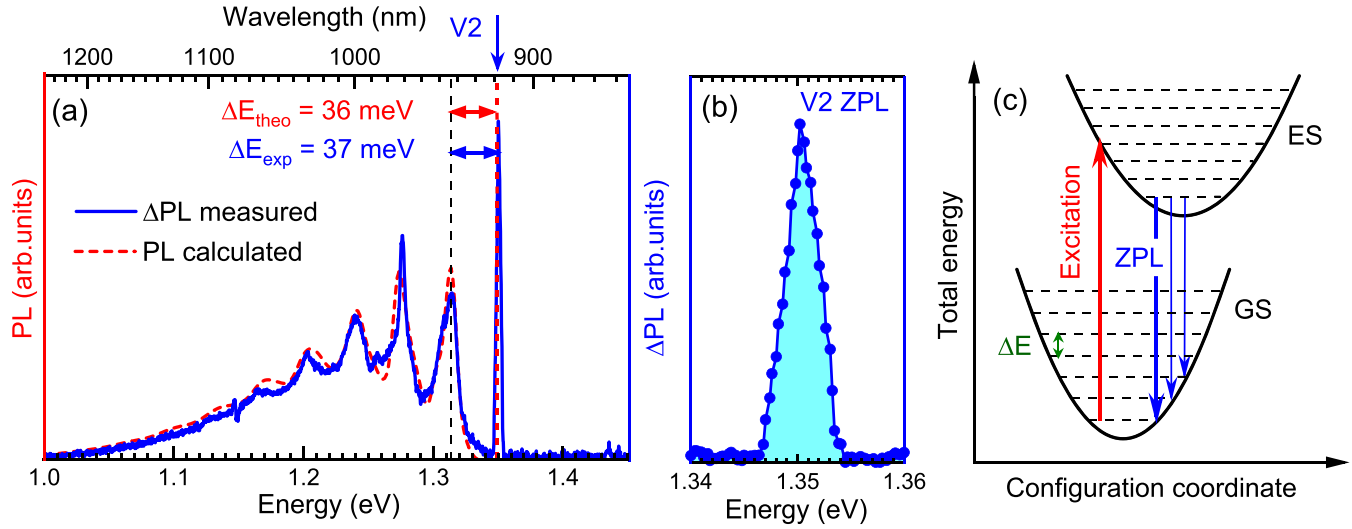

FIG. 4. (a) Low-temperature ($T = 15$ K) ΔPL of V2 as a function of the detection wavelength at the MW frequency of 70 MHz. The vertical axis for PL is the lock-in voltage of the modulated photodiode signal. The V2 ZPL (at 1.35 eV) and PSB are clearly resolved. The local vibrational energy read from two adjacent peaks is $\Delta E_{\rm exp} = 37$ meV. The dashed line represents the calculation of the V2 PSB as described in the text. (b) Zoom-in of the V2 ZPL. (c) A configuration coordinate diagram for the V2 phonon modes. The blue arrows show transitions from the ES to different vibrational levels of the GS.

The HSE functional has been shown to reproduce intradefect transition energies very well [64]. The calculated band gap of 3.25 eV is in excellent agreement with the experimental gap of 3.2 eV [65].

Theoretically, the determination of the average numbers of active phonons during the optical transition for mode λ with frequency ω_λ is given by the unitless partial Huang-Rhys (HR) factor S_λ defined as [48,66]

$$S_\lambda = \frac{1}{2\hbar}\omega_\lambda \Delta Q_\lambda^2, \tag{2}$$

where

$$\Delta Q_\lambda = \sum_\alpha \sqrt{m_\alpha}[(\mathbf{R}_{e,\alpha} - \mathbf{R}_{g,\alpha}) \cdot \mathbf{u}_\lambda]. \tag{3}$$

Here, $\mathbf{u}_\lambda$ indicates the normalized displacement vector corresponding to mode λ, and m_α is the mass of atom α. $\mathbf{R}_g$ and $\mathbf{R}_e$ are the atomic coordinates in the ground and excited states. Thus, ΔQ_λ describes whether the vibrational mode is parallel to the change in the atomic coordinates. The fundamental spectral density of electron-phonon coupling can be determined as

$$S(\hbar\omega) \approx \sum_\lambda \frac{S_\lambda}{\sigma\sqrt{\pi}} e^{-\frac{(\hbar\omega-\hbar\omega_\lambda)^2}{2\sigma^2}}, \tag{4}$$

where a broadening parameter $\sigma = 5$ meV is considered. It is worth mentioning that we assume the vibrational modes in the ground state and the excited state to be identical, and we use in Eq. (3) the **u** evaluated in the ground state. Once $S(\hbar\omega)$ is calculated, we make use of the method of generating function [48,67] to derive the optical absorption spectrum

$$L(\hbar\omega) = \frac{A\omega^3}{2\pi}\int_{-\infty}^{+\infty} g(t)e^{i\omega t}dt, \tag{5}$$

where the prefactor A is the normalization constant and

$$g(t) = e^{S(t)-S(0)} \tag{6}$$

is the generating function, where $S(t)$ is defined by

$$S(t) = \frac{1}{2}\int d(\hbar\omega)e^{-i\omega t}S(\hbar\omega). \tag{7}$$

We modeled the V_{Si} defect in a large 400-atom supercell using $2 \times 2 \times 2$ meshes for k-point sampling. The V2 defect is considered as V_{Si} at the h site [45], in the -1 charge state, and with spin $S = 3/2$ [5]. The HSE06-calculated Kohn-

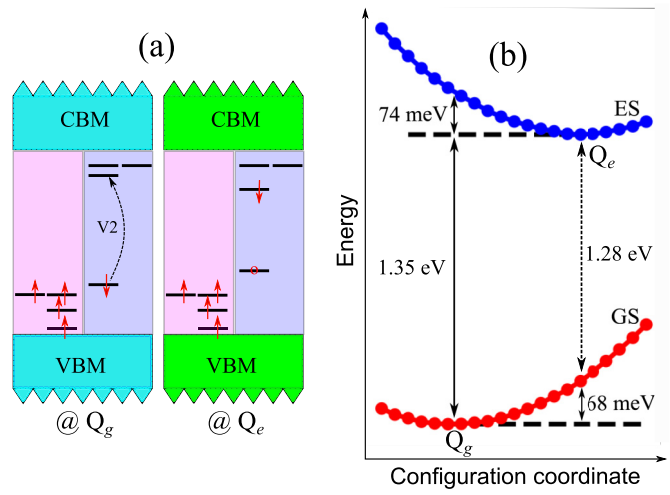

FIG. 5. (a) The arrangement of electronic states before (Q_g) and after (Q_e) excitations calculated using HSE06 functional. The states (dark lines) filled by electrons represented by arrows for spin-up and -down. The hollow circle denotes hole. (b) A schematic configuration coordinate diagram for the GS and ES showing the energy scale for different transitions.

Sham levels are shown in Fig. 5(a), indicating that the V2 defect introduces several electronic states deep in the band gap. The lowest energy electron configuration has the high-spin state with three unpaired electrons ($S = 3/2$). We model the excitation by moving spin-down electrons from the highest occupied to the first unoccupied electronic state, which is achieved by fixing the occupations of the relevant states in the DFT calculations. In the excited state, the two states related to the excitation become closer while others remain the same. From the DFT-calculated total energies we can readily extract the configuration coordinate diagram, as shown in Fig. 5(b). We note that the potential energy curve is calculated using PBEsol, but the ZPL energy difference $[E(Q_g) - E(Q_e)]$ is obtained using HSE06. The emission energy of 1.28 eV and the ZPL of 1.35 eV are in excellent agreement with the experimental values (the former corresponding to the PSB maximum). Introduction of the V2 defect also leads to expansion of the lattice by $\Delta a = 0.083\%$ and $\Delta c = 0.077\%$.

The defects can induce new vibrational modes, which are either resonant or antiresonant with vibrational modes of the host crystal. To map the vibrational modes on the same Brillouin zone as for the pristine SiC, the unfolded phonon

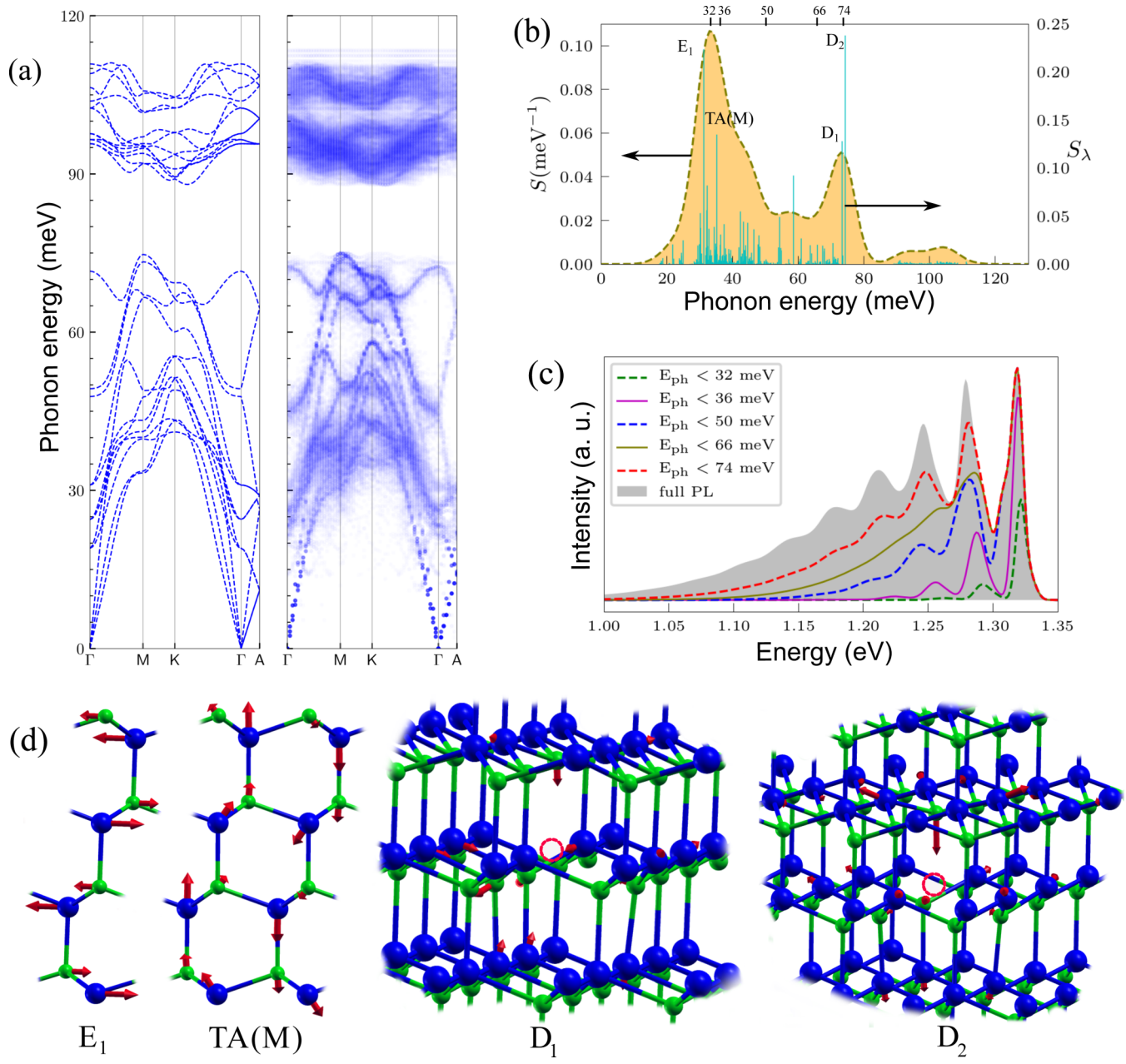

FIG. 6. (a) Pristine SiC phonon dispersion curves and the unfolded phonon curves of defective SiC along high-symmetry directions. (b) Electron-phonon spectral function accompanied by partial Huang-Rhys factors. (c) The calculated partial PSB in the energy range of 1.0–1.35 eV. (d) Schematic representations of atomic displacements of E_1, TA(M), D_1, and D_2 modes. Blue and green balls denote silicon and carbon atoms, respectively. Arrows are proportional to the displacements and come from the real part of the eigenvectors at the Γ point. The defect site is shown by a red circle.

dispersion curve is illustrated in Fig. 6(a). We find that (i) the phonons between 20–40 meV and 90–110 meV are disturbed by the defects, but still follow the dispersion of the bands seen in the pristine system, and (ii) four localized vibrational modes (flat bands) appear at energies 73.45, 74.4, 111.47, and 112.8 meV. To find active phonons during the emission process, the electron-phonon spectral function is calculated as shown in Fig. 6(b). Our calculation predicts that the PSB can be produced by a mix of about four phonon replicas: the double-degenerate Raman-active E_1 mode with energy 31.3 meV, the M-point transverse acoustic phonon active at 35.3 meV, and two defect modes appearing at energies 73.45 and 74.4 meV, denoted as D_1 and D_2, respectively. As illustrated in Fig 6(d), in D_1 defect mode atoms up to second-nearest silicon neighbors from the vacancy center move, while for the D_2 case, vibration is more intense and partially includes third-nearest silicon atoms.

The partial HR factor (S_λ) is the average number of phonon λ emitted during an optical transition. We predict the total HR factor $S = 2.785$, which corresponds to the average number of phonons emitted during an optical transition. As a result, the weight of the ZPL (DW factor) defined by $w_{ZPL} = e^{-S}$ is 6.17%, which is close to our measured value. As was illustrated in Fig. 4(a), our prediction for the PL line shape is in full agreement with the experiments. The PSB with seven peaks falls off at around 1.1 eV.

Following the analysis of vibrational modes, both bulk and defect phonons should contribute to the PSB. To get more insight into line shape, we calculate the partial PSB line shape. To do this, we include phonons up to a specific energy in $S(\hbar\omega)$. The phonon energy (E_{ph}) is chosen based on the values of partial HR factors. In this way, we can assess the contribution of different phonons to the total line shape. As seen in Fig. 6(c), the first peak shape is completed by adding phonons up to 50 meV, but it quickly vanishes at lower energies. At this range of energy we have bulk phonons. The position of the first peak is at 36 meV lower than the ZPL, which is in agreement with the experiments. The comparison of the $E_{\text{ph}} < 66$ meV and full PL curves indicates that a little more than half of the second phonon peak intensity at 1.275 eV (75 meV below the ZPL) arises from two-phonon or higher-order processes, while a little less than half of the peak intensity comes from one-phonon processes with E_{ph}. Furthermore, the defect-induced phonons at around 74 meV are crucial in shaping the second and higher phonon peaks of the optical emission spectrum at low temperature.

IV. DISCUSSION AND CONCLUSIONS

Though the DW factor of 40% and 30% was reported for the V1 and V2 V_{Si} defects, respectively [49,50], the actual value is smaller due to the low detection efficiency at longer wavelengths of the PSB. We experimentally estimated the lower bound for the DW factor of 6%–9%. On the other hand, the calculations also yielded the DW factor of about 6%, which suggests that the real value is indeed in this range. Though this value is at least by a factor of 2 larger than that of the nitrogen vacancy defect in diamond [48], coupling to an optical resonator is necessary to realize quantum repeaters [68]. The vibrational energies of 37 and 36 meV from experiments and calculations, respectively, are also in close agreement. This is an important parameter, which determines at which temperature the phonon-assisted spin-lattice relaxation mechanism associated with local vibrational modes is activated [24].

To summarize, we have investigated the local vibrational structure of the V2 V_{Si} defect in a HPSI 4H-SiC wafer. The MW-assisted spectroscopy has enabled us to clearly separate the spectrally overlapped contribution from other intrinsic defects. We have found the resonant vibrational energy to be 36 meV and have estimated the lower bound for the DW factor to be 6%. We have applied DFT-based methodology to calculate and analyze the PL line shape. Besides that, we have established that the contribution to the optical emission process is narrowed down to dominant bulk and defect-induced phonons. All together, the perfect agreement between the experimental data and the theoretical calculations shows that our approach can be applied to a large number of highly promising optically addressable spin qubits in all stable SiC polytypes, including vacancies [3], divacancies [69], and transition metal color centers [70,71]. It is especially important when the spectral contribution from different defects is overlapped and cannot be separated otherwise. The interaction of local vibrational modes with point defects allows us to understand the spin, optical, mechanical, and thermal properties of these defects. This is crucial for designing defect spins for quantum technologies. We believe that our results present considerable interest for the experimental research of defect-related spin-vibrational properties, while the developed techniques should become an important tool to study a large variety of defects in wide-band-gap semiconducting bulk and two-dimensional materials [72].

Note added. Recently, we became aware of similar research into the vibronic states of the silicon vacancy qubits in SiC [73]. This work applies other experimental and theoretical methods to arrive at an estimate of the DW factor very similar to the estimate in this paper, which speaks in favor of the validity of both approaches.

ACKNOWLEDGMENTS

This work has been supported by the German Research Foundation (DFG) under Grant No. AS 310/5-1 and the Academy of Finland under Projects No. 286279 and No. 311058. We also thank CSC-IT Center Science Ltd., Finland, and HLRS, Stuttgart, Germany for generous grants of computer time. Z.S. thanks the China Scholarship Council (CSC File No. 201706220060) for support. The authors thank R. Narkowicz and K. Lenz for designing and characterization of the coplanar waveguides.

[1] P. G. Baranov, A. P. Bundakova, A. A. Soltamova, S. B. Orlinskii, I. V. Borovykh, R. Zondervan, R. Verberk, and J. Schmidt, Silicon vacancy in SiC as a promising quantum system for single-defect and

single-photon spectroscopy, Phys. Rev. B **83**, 125203 (2011).

[2] W. F. Koehl, B. B. Buckley, F. J. Heremans, G. Calusine, and D. D. Awschalom, Room temperature coherent control of defect spin qubits in silicon carbide, Nature (London) **479**, 84 (2011).

[3] D. Riedel, F. Fuchs, H. Kraus, S. Väth, A. Sperlich, V. Dyakonov, A. A. Soltamova, P. G. Baranov, V. A. Ilyin, and G. V. Astakhov, Resonant Addressing and Manipulation of Silicon Vacancy Qubits in Silicon Carbide, Phys. Rev. Lett. **109**, 226402 (2012).

[4] V. A. Soltamov, A. A. Soltamova, P. G. Baranov, and I. I. Proskuryakov, Room Temperature Coherent Spin Alignment of Silicon Vacancies in 4H- and 6H-SiC, Phys. Rev. Lett. **108**, 226402 (2012).

[5] H. Kraus, V. A. Soltamov, D. Riedel, S. Väth, F. Fuchs, A. Sperlich, P. G. Baranov, V. Dyakonov, and G. V. Astakhov, Room-temperature quantum microwave emitters based on spin defects in silicon carbide, Nat. Phys. **10**, 157 (2014).

[6] S. Castelletto, B. C. Johnson, V. Ivády, N. Stavrias, T. Umeda, A. Gali, and T. Ohshima, A silicon carbide room-temperature single-photon source, Nat. Mater. **13**, 151 (2013).

[7] D. J. Christle, A. L. Falk, P. Andrich, P. V. Klimov, J. Ul Hassan, N. T. Son, E. Janzén, T. Ohshima, and D. D. Awschalom, Isolated electron spins in silicon carbide with millisecond coherence times, Nat. Mater. **14**, 160 (2015).

[8] M. Widmann, S.-Y. Lee, T. Rendler, N. T. Son, H. Fedder, S. Paik, L.-P. Yang, N. Zhao, S. Yang, I. Booker, A. Denisenko, M. Jamali, S. A. Momenzadeh, I. Gerhardt, T. Ohshima, A. Gali, E. Janzén, and J. Wrachtrup, Coherent control of single spins in silicon carbide at room temperature, Nat. Mater. **14**, 164 (2015).

[9] F. Fuchs, B. Stender, M. Trupke, D. Simin, J. Pflaum, V. Dyakonov, and G. V. Astakhov, Engineering near-infrared single-photon emitters with optically active spins in ultrapure silicon carbide, Nat. Commun. **6**, 7578 (2015).

[10] H. Kraus, V. A. Soltamov, F. Fuchs, D. Simin, A. Sperlich, P. G. Baranov, G. V. Astakhov, and V. Dyakonov, Magnetic field and temperature sensing with atomic-scale spin defects in silicon carbide, Sci. Rep. **4**, 5303 (2014).

[11] D. Simin, F. Fuchs, H. Kraus, A. Sperlich, P. G. Baranov, G. V. Astakhov, and V. Dyakonov, High-Precision Angle-Resolved Magnetometry with Uniaxial Quantum Centers in Silicon Carbide, Phys. Rev. Appl. **4**, 014009 (2015).

[12] D. Simin, V. A. Soltamov, A. V. Poshakinskiy, A. N. Anisimov, R. A. Babunts, D. O. Tolmachev, E. N. Mokhov, M. Trupke, S. A. Tarasenko, A. Sperlich, P. G. Baranov, V. Dyakonov, and G. V. Astakhov, All-Optical dc Nanotesla Magnetometry Using Silicon Vacancy Fine Structure in Isotopically Purified Silicon Carbide, Phys. Rev. X **6**, 031014 (2016).

[13] M. Niethammer, M. Widmann, S.-Y. Lee, P. Stenberg, O. Kordina, T. Ohshima, N. T. Son, E. Janzén, and J. Wrachtrup, Vector Magnetometry Using Silicon Vacancies in 4H-SiC Under Ambient Conditions, Phys. Rev. Appl. **6**, 034001 (2016).

[14] C. J. Cochrane, J. Blacksberg, M. A. Anders, and P. M. Lenahan, Vectorized magnetometer for space applications using electrical readout of atomic scale defects in silicon carbide, Sci. Rep. **6**, 37077 (2016).

[15] Ö. O. Soykal and T. L. Reinecke, Quantum metrology with a single spin-3/2 defect in silicon carbide, Phys. Rev. B **95**, 081405(R) (2017).

[16] V. A. Soltamov, C. Kasper, A. V. Poshakinskiy, A. N. Anisimov, E. N. Mokhov, A. Sperlich, S. A. Tarasenko, P. G. Baranov, G. V. Astakhov, and V. Dyakonov, Excitation and coherent control of spin qudit modes in silicon carbide at room temperature, Nat. Commun. **10**, 1678 (2019).

[17] G. Wolfowicz, C. P. Anderson, S. J. Whiteley, and D. D. Awschalom, Heterodyne detection of radio-frequency electric fields using point defects in silicon carbide, Appl. Phys. Lett. **115**, 043105 (2019).

[18] A. N. Anisimov, D. Simin, V. A. Soltamov, S. P. Lebedev, P. G. Baranov, G. V. Astakhov, and V. Dyakonov, Optical thermometry based on level anticrossing in silicon carbide, Sci. Rep. **6**, 33301 (2016).

[19] Y. Zhou, J. Wang, X. Zhang, K. Li, J. Cai, and W. Gao, Self-Protected Thermometry with Infrared Photons and Defect Spins in Silicon Carbide, Phys. Rev. Appl. **8**, 044015 (2017).

[20] L.-P. Yang, C. Burk, M. Widmann, S.-Y. Lee, J. Wrachtrup, and N. Zhao, Electron spin decoherence in silicon carbide nuclear spin bath, Phys. Rev. B **90**, 241203(R) (2014).

[21] S. G. Carter, Ö. O. Soykal, P. Dev, S. E. Economou, and E. R. Glaser, Spin coherence and echo modulation of the silicon vacancy in 4H-SiC at room temperature, Phys. Rev. B **92**, 161202(R) (2015).

[22] H. Seo, A. L. Falk, P. V. Klimov, K. C. Miao, G. Galli, and D. D. Awschalom, Quantum decoherence dynamics of divacancy spins in silicon carbide, Nat. Commun. **7**, 12935 (2016).

[23] J. S. Embley, J. S. Colton, K. G. Miller, M. A. Morris, M. Meehan, S. L. Crossen, B. D. Weaver, E. R. Glaser, and S. G. Carter, Electron spin coherence of silicon vacancies in proton-irradiated 4H-SiC, Phys. Rev. B **95**, 045206 (2017).

[24] D. Simin, H. Kraus, A. Sperlich, T. Ohshima, G. V. Astakhov, and V. Dyakonov, Locking of electron spin coherence above 20 ms in natural silicon carbide, Phys. Rev. B **95**, 161201(R) (2017).

[25] M. Fischer, A. Sperlich, H. Kraus, T. Ohshima, G. V. Astakhov, and V. Dyakonov, Highly Efficient Optical Pumping of Spin Defects in Silicon Carbide for Stimulated Microwave Emission, Phys. Rev. Appl. **9**, 054006 (2018).

[26] S. E. Economou and P. Dev, Spin-photon entanglement interfaces in silicon carbide defect centers, Nanotechnology **27**, 504001 (2016).

[27] D. J. Christle, P. V. Klimov, C. F. de las Casas, K. Szász, V. Ivády, V. Jokubavicius, J. Ul Hassan, M. Syväjärvi, W. F. Koehl, T. Ohshima, N. T. Son, E. Janzén, Á. Gali, and D. D. Awschalom, Isolated Spin Qubits in SiC with a High-Fidelity Infrared Spin-to-Photon Interface, Phys. Rev. X **7**, 021046 (2017).

[28] R. Nagy, M. Niethammer, M. Widmann, Y.-C. Chen, P. Udvarhelyi, C. Bonato, J. Ul Hassan, R. Karhu, I. G. Ivanov, N. T. Son, J. R. Maze, T. Ohshima, Ö. O. Soykal, Á. Gali, S.-Y. Lee, F. Kaiser, and J. Wrachtrup, High-fidelity spin and optical control of single silicon-vacancy centres in silicon carbide, Nat. Commun. **10**, 1954 (2019).

[29] P. Udvarhelyi, R. Nagy, F. Kaiser, S.-Y. Lee, J. Wrachtrup, and A. Gali, Spectrally Stable Defect Qubits with no Inversion Symmetry for Robust Spin-To-Photon Interface, Phys. Rev. Appl. **11**, 044022 (2019).

[30] N. Morioka, C. Babin, R. Nagy, I. Gediz, E. Hesselmeier, D. Liu, M. Joliffe, M. Niethammer, D. Dasari, V. Vorobyov, R. Kolesov, R. Stöhr, J. Ul Hassan, N. T. Son, T. Ohshima,

P. Udvarhelyi, G. Thiering, A. Gali, J. Wrachtrup, and F. Kaiser, Spin-controlled generation of indistinguishable and distinguishable photons from silicon vacancy centres in silicon carbide, arXiv:2001.02455.

[31] H. Kraus, D. Simin, C. Kasper, Y. Suda, S. Kawabata, W. Kada, T. Honda, Y. Hijikata, T. Ohshima, V. Dyakonov, and G. V. Astakhov, Three-dimensional proton beam writing of optically active coherent vacancy spins in silicon carbide, Nano Lett. **17**, 2865 (2017).

[32] J. Wang, X. Zhang, Y. Zhou, K. Li, Z. Wang, P. Peddibhotla, F. Liu, S. Bauerdick, A. Rudzinski, Z. Liu, and W. Gao, Scalable fabrication of single silicon vacancy defect arrays in silicon carbide using focused ion beam, ACS Photonics **4**, 1054 (2017).

[33] J.-F. Wang, Q. Li, F.-F. Yan, H. Liu, G.-P. Guo, W.-P. Zhang, X. Zhou, L.-P. Guo, Z.-H. Lin, J.-M. Cui, X.-Y. Xu, J.-S. Xu, C.-F. Li, and G.-C. Guo, On-demand generation of single silicon vacancy defects in silicon carbide, ACS Photonics **6**, 1736 (2019).

[34] F. Fuchs, V. A. Soltamov, S. Väth, P. G. Baranov, E. N. Mokhov, G. V. Astakhov, and V. Dyakonov, Silicon carbide light-emitting diode as a prospective room temperature source for single photons, Sci. Rep. **3**, 1637 (2013).

[35] A. Lohrmann, N. Iwamoto, Z. Bodrog, S. Castelletto, T. Ohshima, T. J. Karle, A. Gali, S. Prawer, J. C. McCallum, and B. C. Johnson, Single-photon emitting diode in silicon carbide, Nat. Commun. **6**, 7783 (2015).

[36] S.-i. Sato, T. Honda, T. Makino, Y. Hijikata, S.-Y. Lee, and T. Ohshima, Room Temperature Electrical Control of Single Photon Sources at 4H-SiC Surface, ACS Photonics **5**, 3159 (2018).

[37] M. Widmann, M. Niethammer, T. Makino, T. Rendler, S. Lasse, T. Ohshima, J. Ul Hassan, N. Tien Son, S.-Y. Lee, and J. Wrachtrup, Bright single photon sources in lateral silicon carbide light emitting diodes, Appl. Phys. Lett. **112**, 231103 (2018).

[38] P. V. Klimov, A. L. Falk, B. B. Buckley, and D. D. Awschalom, Electrically Driven Spin Resonance in Silicon Carbide Color Centers, Phys. Rev. Lett. **112**, 087601 (2014).

[39] A. L. Falk, P. V. Klimov, B. B. Buckley, V. Ivády, I. A. Abrikosov, G. Calusine, W. F. Koehl, A. Gali, and D. D. Awschalom, Electrically and Mechanically Tunable Electron Spins in Silicon Carbide Color Centers, Phys. Rev. Lett. **112**, 187601 (2014).

[40] M. Widmann, M. Niethammer, D. Y. Fedyanin, I. A. Khramtsov, T. Rendler, I. D. Booker, J. Ul Hassan, N. Morioka, Y.-C. Chen, I. G. Ivanov, N. T. Son, T. Ohshima, M. Bockstedte, A. Gali, C. Bonato, S.-Y. Lee, and J. Wrachtrup, Electrical charge state manipulation of single silicon vacancies in a silicon carbide quantum optoelectronic device, Nano Lett. **19**, 7173 (2019).

[41] S. J. Whiteley, G. Wolfowicz, C. P. Anderson, A. Bourassa, H. Ma, M. Ye, G. Koolstra, K. J. Satzinger, M. V. Holt, F. J. Heremans, A. N. Cleland, D. I. Schuster, G. Galli, and D. D. Awschalom, Spin–phonon interactions in silicon carbide addressed by Gaussian acoustics, Nat. Phys. **15**, 490 (2019).

[42] A. V. Poshakinskiy and G. V. Astakhov, Optically detected spin-mechanical resonance in silicon carbide membranes, Phys. Rev. B **100**, 094104 (2019).

[43] S. Castelletto, B. C. Johnson, C. Zachreson, D. Beke, I. Balogh, T. Ohshima, I. Aharonovich, and A. Gali, Room temperature quantum emission from cubic silicon carbide nanoparticles, ACS Nano **8**, 7938 (2014).

[44] A. Muzha, F. Fuchs, N. V. Tarakina, D. Simin, M. Trupke, V. A. Soltamov, E. N. Mokhov, P. G. Baranov, V. Dyakonov, A. Krueger, and G. V. Astakhov, Room-temperature near-infrared silicon carbide nanocrystalline emitters based on optically aligned spin defects, Appl. Phys. Lett. **105**, 243112 (2014).

[45] E. Sörman, N. T. Son, W. M. Chen, O. Kordina, C. Hallin, and E. Janzén, Silicon vacancy related defect in 4H and 6H SiC, Phys. Rev. B **61**, 2613 (2000).

[46] N. T. Son, P. Carlsson, J. Ul Hassan, E. Janzén, T. Umeda, J. Isoya, A. Gali, M. Bockstedte, N. Morishita, T. Ohshima, and H. Itoh, Divacancy in 4H-SiC, Phys. Rev. Lett. **96**, 055501 (2006).

[47] A. Gali, T. Simon, and J. E. Lowther, An *ab initio* study of local vibration modes of the nitrogen-vacancy center in diamond, New J. Phys. **13**, 025016 (2011).

[48] A. Alkauskas, B. B. Buckley, D. D. Awschalom, and C. G. Van de Walle, First-principles theory of the luminescence lineshape for the triplet transition in diamond NV centres, New J. Phys. **16**, 073026 (2014).

[49] R. Nagy, M. Widmann, M. Niethammer, D. B. R. Dasari, I. Gerhardt, Ö. O. Soykal, M. Radulaski, T. Ohshima, J. Vučković, N. T. Son, I. G. Ivanov, S. E. Economou, C. Bonato, S.-Y. Lee, and J. Wrachtrup, Quantum Properties of Dichroic Silicon Vacancies in Silicon Carbide, Phys. Rev. Appl. **9**, 034022 (2018).

[50] H. B. Banks, Ö. O. Soykal, R. L. Myers-Ward, D. K. Gaskill, T. L. Reinecke, and S. G. Carter, Resonant Optical Spin Initialization and Readout of Single Silicon Vacancies in 4H-SiC, Phys. Rev. Appl. **11**, 024013 (2019).

[51] Ö. O. Soykal, P. Dev, and S. E. Economou, Silicon vacancy center in 4H-SiC: Electronic structure and spin-photon interfaces, Phys. Rev. B **93**, 081207(R) (2016).

[52] V. Ivády, I. A. Abrikosov, and A. Gali, First principles calculation of spin-related quantities for point defect qubit research, npj Comput. Mater. **4**, 45 (2018).

[53] M. Bockstedte, F. Schütz, T. Garratt, V. Ivády, and A. Gali, *Ab initio* description of highly correlated states in defects for realizing quantum bits, npj Quantum Mater. **3**, 5645 (2018).

[54] V. Ivády, J. Davidsson, N. T. Son, T. Ohshima, I. A. Abrikosov, and A. Gali, Identification of Si-vacancy related room-temperature qubits in 4H silicon carbide, Phys. Rev. B **96**, 161114(R) (2017).

[55] J. R. Weber, W. F. Koehl, J. B. Varley, A. Janotti, B. B. Buckley, C. G. Van de Walle, and D. D. Awschalom, Quantum computing with defects, Proc. Natl. Acad. Sci. U.S.A. **107**, 8513 (2010).

[56] W. Dong, M. W. Doherty, and S. E. Economou, Spin polarization through intersystem crossing in the silicon vacancy of silicon carbide, Phys. Rev. B **99**, 184102 (2019).

[57] M. A. Reshchikov, A. A. Kvasov, M. F. Bishop, T. McMullen, A. Usikov, V. Soukhoveev, and V. A. Dmitriev, Tunable and abrupt thermal quenching of photoluminescence in high-resistivity Zn-doped GaN, Phys. Rev. B **84**, 075212 (2011).

[58] C. Kittel, *Introduction to Solid State Physics* (Wiley, New York, 2004).

[59] G. Kresse and J. Hafner, *Ab initio* molecular dynamics for liquid metals, Phys. Rev. B **47**, 558 (1993).

[60] J. P. Perdew, A. Ruzsinszky, G. I. Csonka, O. A. Vydrov, G. E. Scuseria, L. A. Constantin, X. Zhou, and K. Burke, Restoring the Density-Gradient Expansion for Exchange in Solids and Surfaces, Phys. Rev. Lett. **100**, 136406 (2008).

[61] F. Eriksson, E. Fransson, and P. Erhart, The hiphive package for the extraction of high-order force constants by machine learning, Adv. Theory Simul. **2**, 1800184 (2019).

[62] A. Togo and I. Tanaka, First principles phonon calculations in materials science, Scr. Mater. **108**, 1 (2015).

[63] A. V. Krukau, O. A. Vydrov, A. F. Izmaylov, and G. E. Scuseria, Influence of the exchange screening parameter on the performance of screened hybrid functionals, J. Chem. Phys. **125**, 224106 (2006).

[64] P. Deák, B. Aradi, T. Frauenheim, E. Janzén, and A. Gali, Accurate defect levels obtained from the HSE06 range-separated hybrid functional, Phys. Rev. B **81**, 153203 (2010).

[65] A. A. Lebedev, Deep level centers in silicon carbide: A review, Semiconductors **33**, 107 (1999).

[66] J. J. Markham, Interaction of normal modes with electron traps, Rev. Mod. Phys. **31**, 956 (1959).

[67] T. Miyakawa and D. L. Dexter, Phonon sidebands, multiphonon relaxation of excited states, and phonon-assisted energy transfer between ions in solids, Phys. Rev. B **1**, 2961 (1970).

[68] D. M. Lukin, C. Dory, M. A. Guidry, K. Y. Yang, S. D. Mishra, R. Trivedi, M. Radulaski, S. Sun, D. Vercruysse, G. H. Ahn, and J. Vučković, 4H-silicon-carbide-on-insulator for integrated quantum and nonlinear photonics, Nat. Photonics (2019), doi:10.1038/s41566-019-0556-6.

[69] A. L. Falk, B. B. Buckley, G. Calusine, W. F. Koehl, V. V. Dobrovitski, A. Politi, C. A. Zorman, P. X. L. Feng, and D. D. Awschalom, Polytype control of spin qubits in silicon carbide, Nat. Commun. **4**, 1819 (2013).

[70] S. A. Zargaleh, B. Eble, S. Hameau, J. L. Cantin, L. Legrand, M. Bernard, F. Margaillan, J. S. Lauret, J. F. Roch, H. J. von Bardeleben, E. Rauls, U. Gerstmann, and F. Treussart, Evidence for near-infrared photoluminescence of nitrogen vacancy centers in 4H-SiC, Phys. Rev. B **94**, 060102(R) (2016).

[71] W. F. Koehl, B. Diler, S. J. Whiteley, A. Bourassa, N. T. Son, E. Janzén, and D. D. Awschalom, Resonant optical spectroscopy and coherent control of Cr^{4+} spin ensembles in SiC and GaN, Phys. Rev. B **95**, 035207 (2017).

[72] A. Gottscholl, M. Kianinia, V. Soltamov, S. Orlinskii, G. Mamin, C. Bradac, C. Kasper, K. Krambrock, A. Sperlich, M. Toth, I. Aharonovich, and V. Dyakonov, Initialization and read-out of intrinsic spin defects in a van der Waals crystal at room temperature, Nat. Mater. **19**, 540 (2020).

[73] P. Udvarhelyi, G. Thiering, N. Morioka, C. Babin, F. Kaiser, D. Lukin, T. Ohshima, J. Ul Hassan, N. T. Son, J. Vučković, J. Wrachtrup, and A. Gali, Vibronic states and their effect on the temperature and strain dependence of silicon-vacancy qubits in 4H silicon carbide, arXiv:2001.02459 [Phys. Rev. Appl. (to be published)].